Biochimica et Biophysica Acta 1861 (2017) 910–921

Contents lists available at ScienceDirect

Biochimica et Biophysica Acta

journal homepage: www.elsevier.com/locate/bbagen

Binding of Amphipathic Cell Penetrating Peptide p28 to Wild Type and Mutated p53 as studied by Raman, Atomic Force and Surface Plasmon Resonance spectroscopies

Sara Signorelli [a,b,1], Simona Santini [a,1], Tohru Yamada [c], Anna Rita Bizzarri [a,*], Craig W. Beattie [c], Salvatore Cannistraro [a]

[a] Biophysics and Nanoscience Centre, DEB, Università della Tuscia, Viterbo, Italy
[b] Department of Science, University Roma Tre, Rome, Italy
[c] Department of Surgery, Division of Surgical Oncology, University of Illinois College of Medicine, Chicago, IL, USA

ARTICLE INFO

Article history:
Received 24 August 2016
Received in revised form 21 December 2016
Accepted 20 January 2017
Available online 24 January 2017

Keywords:
Raman spectroscopy
Atomic Force Spectroscopy
Docking
p53
Mutations
Cell penetrating peptide

ABSTRACT

Background: Mutations within the DNA binding domain (DBD) of the tumor suppressor p53 are found in >50% of human cancers and may significantly modify p53 secondary structure impairing its function. p28, an amphipathic cell-penetrating peptide, binds to the DBD through hydrophobic interaction and induces a posttranslational increase in wildtype and mutant p53 restoring functionality. We use mutation analyses to explore which elements of secondary structure may be critical to p28 binding.
Methods: Molecular modeling, Raman spectroscopy, Atomic Force Spectroscopy (AFS) and Surface Plasmon Resonance (SPR) were used to identify which secondary structure of site-directed and naturally occurring mutant DBDs are potentially altered by discrete changes in hydrophobicity and the molecular interaction with p28.
Results: We show that specific point mutations that alter hydrophobicity within non-mutable and mutable regions of the p53 DBD alter specific secondary structures. The affinity of p28 was positively correlated with the β-sheet content of a mutant DBD, and reduced by an increase in unstructured or random coil that resulted from a loss in hydrophobicity and redistribution of surface charge.
Conclusions: These results help refine our knowledge of how mutations within p53-DBD alter secondary structure and provide insight on how potential structural alterations in p28 or similar molecules improve their ability to restore p53 function.
General significance: Raman spectroscopy, AFS, SPR and computational modeling are useful approaches to characterize how mutations within the p53DBD potentially affect secondary structure and identify those structural elements prone to influence the binding affinity of agents designed to increase the functionality of p53.

1. Introduction

Tumor suppressor protein p53 (TP53) is a homotetramer with each monomer composed of an N-terminal transactivation domain (NTD, a.a. residues 1–70), a folded DNA-binding (DBD, residues 94–293) that, in reality, is substantially more flexible than apparent from crystal structures and a regulatory domain in the C-terminus (CTD, residues 324–355) [1–3]. When unbounded, p53 populates an ensemble of diverse, interconverting, and thermodynamic stable conformations that confer significant inherent flexibility and allow this single protein to recognize a large number of biological targets without sacrificing specificity [4,5]. The N- and C-terminal regions of p53 are intrinsically unfolded, but can form a compact secondary structure when interacting with partner proteins [2,3]. Although the DBD is intrinsically structured, at physiological temperatures in the absence of modifications or stabilizing partners, wild-type p53 is >50% unfolded correlating with a 75% loss in DNA-binding activity [2]. The overall NMR structure of p53 core domain is a β-sandwich, composed of two antiparallel β-sheets with a small β-hairpin (124–135) in contact with a second β-sheet, closing the access to the hydrophobic core [2,3]. The β-sandwich serves as a scaffold for two large loops and a loop-sheet-helix motif that form the DNA binding surface of p53. These latter motifs represent conserved regions of the core domain and contain mutations that potentially inactivate p53 in some 50% of human cancers [1,6,7]. A limited number of these localized mutations appear repeatedly as *hotspots* and either affect residues directly in contact with DNA (R248 or R273) or distort overall protein folding (R175, G245, R249 and R282) [8].

* Corresponding author at: Biophysics and Nanoscience Centre, Università della Tuscia, Viterbo, Italy.
E-mail address: bizzarri@unitus.it (A.R. Bizzarri).
[1] These authors have equally contributed to the work.

http://dx.doi.org/10.1016/j.bbagen.2017.01.022
0304-4165/

Some mutations also produce oncogenic, gain-of-function, like properties as a result of constitutive stabilization that promote malignant progression, invasion and metastases and chemoresistance [9–11] while most apparently result in a protein that is unable to promote the transcription of (all) the multiple genes regulated by wild type p53 [12,13]. However, ~30% of recorded mutations among over 30,500 known mutations in the *p53* gene (www-p53.iarc.fr) retain at least some transcriptional function including an altered transactivation specificity [14]. Structural studies on the p53 DBD are therefore currently focused on whether and how native conformations are modified by mutations; possibly in order to revert them and restore physiological activity to transformed cells [15–17].

Several small molecules that either restore a wild-type conformation and transcriptional activity or induce synthetic lethality to mutant p53 have been synthesized. Only one, that binds to thiol groups within the p53 core domain (DBD) to restore a wild-type conformation, currently remains in clinical trial for advanced cancers [18]. All appear to have significant clinical toxicity.

In contrast, we and others demonstrated that azurin [19–23] and a nontoxic 28 amino acid fragment (aa 50–77), p28, of this copper containing, redox protein bind with high affinity to the DBD of p53 [24] without altering its overall conformation [25,26]. The majority of p28 binding sites are within the non-mutable L_1 loop (aa 112–124) [27–29] and a mutable region *e.g.* Y220C, P223L within the S_{7-8} loops (aa 214–236) of the DBD [25]. Missense mutations that do not prevent DNA contact or completely unfold the molecule generally do not inhibit a p28 induced post-translational increase in wild type ($p53^{wt}$) or mutated ($p53^{mut}$) p53 and accompanying decrease in the downstream cell cycle inhibitor p21 [25,26,30] in a wide variety of cancer cells, nor elicit a deleterious *gain-of-function* via either p63 or p73 [31]. We have also shown that some *hotspot* missense mutations within the p53 DBD that prevent contact with DNA do not necessarily inhibit the post-translational increase in p53 induced by p28 [26], but the accompanying p28 induced decrease in the downstream cell cycle inhibitor p21, is lost [25,26,30]. This suggests that when secondary structure, surface charge and conformational integrity is essentially maintained, p28 continues to induce an increase in the level of either $p53^{wt}$ or $p53^{mut}$.

Protein structure and conformation are governed primarily by internal hydrophobic effects and by interactions between polar residues and other types of bonds with the hydrophobic effect a major determinant of original protein structure.

Molecular dynamics simulations, computational docking and cluster analyses predict that hydrophobicity as well as secondary structure may play a significant role in the binding of p28 to the L_1 and S_{7-8} loops of the p53 DBD [26–32]. We have also shown that the linear combination of signals for each structural conformation of p28 by Raman spectroscopy provides an "instantaneous snapshot" [33] of this anionic, amphipathic peptide during its transition through the cancer cell membrane [34]. This suggested that dissection of the Amide I Raman band to reveal the amount of α-helix, β-sheet and random coil present in known structural mutations within the wild type p53 DBD of cancer cells [35], coupled with an analysis of single point mutations that produce hydrophobic to hydrophilic changes in normally non-mutable motifs binding p28, would provide insight as to how mutations in p53 might alter the binding of p28 or similar molecules [36].

Atomic Force Spectroscopy, an innovative nanotechnology able to measure very low intermolecular forces between single biological partner couples under physiological conditions and without any labeling [22,24], was applied to determine the binding of p28 to site-specific and naturally occurring DBD mutants, and complement Raman and molecular docking results. Finally, data obtained at single molecule level by AFS, were further assessed by Surface Plasmon Resonance (SPR), a powerful approach providing the kinetic and equilibrium characterization of binding processes occurring between a sensor chip immobilized ligand and its partner free in solution [37].

Overall, we found that mutation induced reductions in the β-sheet content of specific motifs within the p53 DBD are associated with a loss of secondary structure and conformation essential to the integrity of p28 binding to the p53 DBD.

2. Materials and methods

2.1. Sample selection and purification

The wild type-DBD fragment, a.a. 81–300 of p53 ~25 kDa was constructed as described [25,26]. All site-directed mutants were constructed with QuikChange mutagenesis kits (Agilent Technology) and purified as described in ref. [28]. Single point mutations included L114D, A119D and C124D within the L_1 loop and C229D in the S_{7-8} loop designed to produce hydrophobic to hydrophilic changes in the normally non-mutable L_1 motif and within the S_{7-8} loop. These were compared with the wild type DBD (DBD^{wt}) and those naturally occurring single P223L/V274F, that all bind p28, to provide insight as to how mutations that altered hydrophobicity might affect secondary structure and alter the binding of p28 or similar molecules.

2.2. Sample preparation

Methanol (MeOH, CH_3OH) was purchased from Carlo Erba (Carlo Erba Reagent, Milan, IT); 2,2,2 Trifluoroethanol (TFE, CF_3CH_2OH) was obtained from Sigma-Aldrich, St. Louis, MO, USA. The dielectric constant values for PBS, MeOH and TFE were taken to be 78.3, 33.1 and 27.7, respectively [38,39]. All samples were dissolved in phosphate-buffered-saline (PBS, 95.3% H_2O, 3.8% NaCl, 0.1% di KCl, 0.7% Na_2HPO_4, 0.1% KH_2PO_4; pH = 7.5), MeOH (MeOH/PBS, 1:1) and TFE (TFE/PBS, 1:1), reaching a final concentration of 60 μM.

2.3. AFS tip functionalization

The 28 amino acid azurin fragment p28 was bound to silicon nitride AFS tips (Veeco Instruments, Plainview, NY, USA) through a cysteine residue added to its NH_2-terminus to create p29 (Cys-p28, 3.0 kDa) as described [24]. Briefly, the tips were cleaned in acetone at room temperature for 10 min, dried under a stream of nitrogen, and then ultraviolet (UV) irradiated for 30 min to expose hydroxyl groups. Later, they were immersed in a solution of 2% (v/v) of 3-aminopropyl-triethoxysilane (APTES) (Acros Organics, Geel, Belgium) in chloroform in order to functionalize the tip surface with amino groups, incubated for 2 h at room temperature, washed with chloroform and then dried with nitrogen. Silanized tips were successively immersed in 1 mM N-hydroxysuccinimide-polyethylene glycolmaleimide (NHS-PEG-MAL, molecular weight, 1395 Da, 9.5 nm in length (Thermo Scientific Inc., Waltham, MA)) and dissolved in dimethylsulfoxide (DMSO) for 3 h at room temperature. This allows the NHS-ester group at one end of the PEG to react with an amino-silane to form an amide bond while the —MAL group reacts with the —SH group of the cysteine residue conjugated to the NH_2-terminal of p28. After washing with DMSO and Milli-Q® (Millipore, Billerica, MA, USA) water, the tips were incubated with 10 μl of 10 μM p29 in 50 mM phosphate buffered saline (PBS), pH 7.5, overnight at 4 °C. The tips were then gently rinsed and stored in buffer at 4 °C.

2.3.1. AFS substrate

Glass slides were prepared to immobilize wild type and mutant p53 DBDs [24]. Glass substrates were cleaned in acetone for 5 min, dried under a stream of nitrogen, and UV-irradiated for 30 min to expose the —OH groups on their surface. After immersion in 0.3 M APTES in chloroform and incubation for 3 min at room temperature, they were rinsed in three changes of chloroform and dried with nitrogen. Glass slides were subsequently incubated with a solution of 1% glutaraldehyde (Sigma-Aldrich, St Louis, MO, USA) in Milli-Q water for 4 min at

room temperature, rinsed with Milli-Q water, and dried with nitrogen. 50 μl of a 10 μM solution of wild type and mutants p53 DBD in 50 mM PBS pH 7.5 were poured onto this amine-reactive surface, incubated overnight at 4 °C, gently washed with PBS, and stored in buffer at 4 °C.

2.3.2. AFS measurements

Force measurements were carried out in PBS buffer (50 mM K_3PO_4, 150 mM NaCl, pH 7.5) using force calibration mode AFM. The cantilevers had a nominal spring constant, k_{nom}, of 0.02 N/m while the effective spring constant, k_{eff}, was determined as reported [40].

Each force experiment was conducted by recording approaching and retracting force-distance curves. The maximum force exerted by the tip on the proteins substrate was limited to 0.5 nN by applying a relative trigger of 50 nm. A ramp size of 150 nm was set, and an encounter time of 100 ms was established. Tips and substrate were approached at a constant velocity of 50 nm/s, while the retraction velocity was varied from 50 to 4.200 nm/s according to the selected nominal loading rates; these last, defined as the product of the nominal cantilever spring constant (k_{nom}) by the tip pulling velocity (v), set in a nominal range of 1–84 nN/s. The effective loading rate was determined by replacing the nominal cantilever constant with the effective one, k_{syst}, to take into account the change in the cantilever spring constants due to the anchoring of molecules (*e.g.* proteins and/or linkers) to the AFS tip. The k_{syst} values at various loading rates were obtained from the slope of the retraction curve immediately prior to the unbinding event [41]. A thousand force curves were recorded for each loading rate and analyzed as described [24,42,43]. The specificity of each interaction was assessed (blocking experiments) by adding a 30 μM solution of free p28 to the DBD functionalized substrates with a nominal loading rate of 7 nN/s for each experiment. The unbinding force was determined as the product of the cantilever deflection and its effective spring constant k_{eff} from each of the force-curves corresponding to specific unbinding event for each p28 interaction and plotted as a histogram for each loading rate. All histograms showed a single mode distribution indicative of the existence of a single unbinding process, similar to that observed in other systems [44–46]. The most probable unbinding force was determined from the maximum of the main peak of each histogram, 58–95 pN, well within the range reported for other specific biological interactions at a similar loading rate [18]. As the unbinding process measured by AFS takes place under the application of an external force that alters the energy profile of the interaction the kinetic parameters of the biorecognition process at equilibrium were extracted by treating the data under the Bell-Evans model [42,47,48]. To completely characterize the kinetic interaction of p28 binding to the p53 DBD, the association rate constant (k_{on}) was also determined by following the procedure in ref. [49]. Once k_{on} values were calculated, the dissociation equilibrium constant (K_D) for each of the analyzed binding interactions was extracted as $K_D = k_{off} / k_{on}$.

2.4. Raman spectroscopy

A Jobin-Yvon Super Labram confocal system equipped with a liquid nitrogen-cooled CCD (EEV CCD10-11 back illuminated; pixel format: 1024 × 128 detector and a spectrograph with a 1800 g/mm grating allowing a resolution of 5 cm^{-1}) was used to acquire Raman spectra. A filter to reject the elastic contribution and back-scattering geometry for spectra collection was applied. The source was a diode-pumped solid state laser emitting in the green region of the spectrum at 532 nm with a power of 10 mW (4.4 mW on the sample). Measurements were collected using a 50× objective with a numerical aperture NA = 0.6 (laser spot diameter reaching the sample was 1 μm). A confocal diaphragm of 400 μm and a slit of 200 μm were chosen as optimal acquisition parameters. The typical acquisition time was 3 min. Specimen drops (20 μl) were deposited on optical glass for the acquisition. Raman spectra were collected from different points of the drops at room temperature. The whole spectral region (600–1750 cm^{-1}) was normalized through vector normalization in the spectral range of the Amide I band (1525–1750 cm^{-1}); this scaling all the spectra so that their vertical minimum is at zero and the Amide I peak of all spectra match at the same height. This pre-processing method attempts to minimize the variability in the spectra caused by source/environment fluctuations that are not related to the actual differences (chemical or structural) in the samples. Further, all spectra were baseline corrected (70-data point rubber band method) in order to remove the fluorescence background [35].

2.5. Curve fitting

Band fitting of the Raman Amide I mode (1545–1725 cm^{-1}) was performed as previously reported [35]. Briefly, the spectral region between 1620 and 1725 cm^{-1} was fitted with three curves associated with α-helical conformations (1655 cm^{-1}), β-sheet structures (1667 cm^{-1}) and random coiled regions at 1680–1685 cm^{-1} [33,35,50]. A further fitting curve was added at 1645 cm^{-1}, due to a disordered/vibronic coupling band. Spectral peaks at 1550, 1580, 1604, and 1615 cm^{-1} were included to account for Trp, Phe, Tyr and Tyr residues, respectively, since they were not baseline separated from Amide I features. Spectra were normalized with the baseline from 1525 to 1720 cm^{-1} assumed to be linear [35]. Curve-fitting was performed using the Levenberg-Marquardt minimization algorithm (LMA) and a mixture of Lorentzian/Gaussian pseudo-Voigt functions to provide peak profiles. The curve-fitting procedure of the Amide I band was repeated on five different spectra; standard deviations of 10% of the average value were obtained in all the cases. The goodness of the fits was estimated from the reduced chi-square value. All data processing and analysis, including the curve-fitting procedure, were performed with OPUS software v. 6.5.

2.6. Molecular dynamics (MD)

Computer simulations were performed essentially as described [20,21,25]. Conformations for azurin and the DNA-binding domain (DBD) of p53 were taken from PDB files 1E5Z (chain B) and 1UTP (chain A) at 2.0 Å and 2.2 Å resolution, respectively. The 28 aa sequence of p28 was cut from the overall crystallographic structure for azurin and used to generate the configuration file subsequently applied to MD simulations at 300 K and $P = 1$ bar. The Nose–Hoover thermostat method was applied to control the system temperature, with a coupling time constant $t = 0.1$ ps. Constant pressure was imposed using the Parrinello–Rahman extended-ensemble ($P = 1.0$ ps). p28 was minimized with steepest descent and gradually heated from 50 to 300 K at increments of 50 K. The system was then equilibrated by a 600 ps MD simulation under position restraints, prior to an unrestrained MD run for 3 ns. The resulting structure file for p28 was used for further analysis. Amino acid substitutions and internal deletions of p53 DBD present in solid tumor cell lines were modeled using the Schrödinger molecular modeling package [26].

2.7. Docking studies

ClusPro [51] was used to conduct automated docking as a six-dimensional search within the rotational space between two molecules. The docking algorithms of ClusPro evaluate 10^9 putative complexes, retaining a preset number with favorable surface complementarities, after filtering with electrostatic and desolvation free energies for further clustering. The desolvation free energy used the atomic contact potential [52], a statistical measure of the desolvation free energy, with the electrostatic free energy calculated using a Coulombic model with a distance-dependent dielectric of 4r [53]. The top 2000 energetically favorable structures were clustered on the basis of a pairwise binding site root mean squared deviation criterion. Clusters were formed by selecting the ligand that had the most

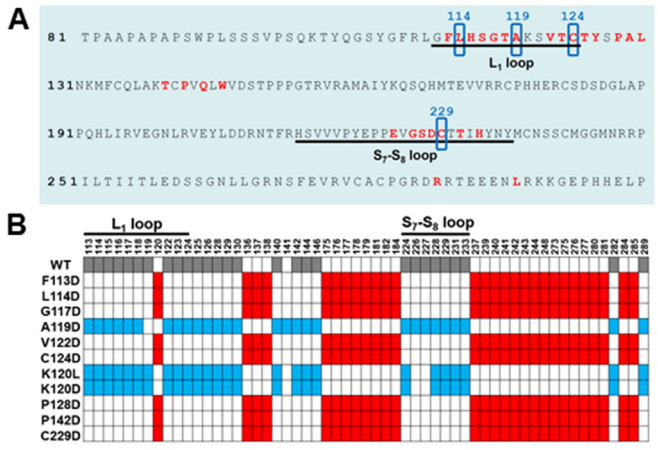

Fig. 1. A. Predicted p28 binding sites within the p53 DNA-binding domain. The L_1 loop (aa 112–124) and S_7–S_8 loop (aa 214–236) are underlined. Predicted p28-binding residues including parts of L_1 and S_7–S_8 loops and R282 and L289 are indicated (red) within the p53 DBD (aa 81–300 of human p53). Site-directed mutations are indicated (blue box). B. Hydrophobic Interactions between p53 DBD and p28. Amino acid residue numbers (top) and substitutions within p53 (left) were modeled using the Schrödinger software package. Docking analyses of potential alterations of p28 binding to $p53^{mut}$ sites relative to $p53^{wt}$ were carried out using the ClusPro 2.0 server. Residues on $p53^{wt}$ binding p28 are gray. Residues on $p53^{mut}$ with >95% identity to $p53^{wt}$ are in blue. Predicted p28 binding sites significantly altered when hydrophobic aa of p53 were mutated to hydrophilic aa are in (red). Substitution of A119 to D did not significantly alter p28 binding sites, suggesting that A119 is not critical to p28 binding.

neighbors below a previously selected clustering radius. Each member within the cluster was eliminated from the matrix to avoid overlaps between clusters that were repeated until at least 30 clusters formed, and the cluster model with the best score was selected to further compare the protein–protein interface using the ProtorP: Protein–Protein Interface Analysis Server [54]. Molecular surfaces and electrostatic potentials of wild type and mutated p53 were calculated by DeepView (Swiss Institute of Bioinformatics) [82].

2.8. Surface plasmon resonance measurements

SPR experiments were carried out at 25 °C by using PBS (50 mM K_3PO_4, 150 mM NaCl, pH 7.5, surfactant P20 0.005% from GE Healthcare) as running buffer. GST-tagged wild type p53 DBD, and physiological p53 DBD mutants, were alternatively coupled to a single channel of a CM5 sensor chip surface (GE Healthcare, Uppsala, Sweden) by following a GST capture procedure. Briefly, anti-GST antibodies (immunosorbent-purified polyclonal goat antibody, 0.6 mg/ml in 0.15 M NaCl, 100 μl) were covalently coupled to both channel of a CM5 sensor chip surface by using a standard amine coupling procedure as described [55]. The carboxyl groups of the sensor chip dextran matrix were activated by a mixture of N-hydroxyl-succinimide (NHS) and N-ethyl-N-(3-dimethylaminopropyl) carbodiimide (EDC). Anti-GST antibody from the GST capture kit (GE Healthcare, Uppsala, Sweden) was thus diluted to 30 μg/ml in immobilization buffer and injected at 10 μl/min for 5 min on both the reference and experimental flow cells. Unreacted NHS-esters were successively blocked by a 1 M ethanolamine-HCl, (pH 8.5, GE Healthcare, Uppsala, Sweden) injection. Polyclonal anti-GST antibody high affinity sites were thus blocked by running 3 cycles of a 3-min injection of recombinant GST (*Schistosoma japonicum*, molecular weight 26 kDa; 0.2 mg/ml in HBS-EP buffer, 0.005% surfactant P20), at 5 μg/ml in running buffer followed by regeneration, by following the GST capture kit protocol. GST-tagged wild type, single point and physiological p53 DBD mutants, diluted in running buffer at a final concentration of 0.5 μM were successively coupled to a single channel of the CM5 sensor chip surface until an immobilization level of about 700 Resonance Unit (RU) was reached. Both the reference and the experimental flow cells were thus saturated by successive injection of GST. The same anti-GST substrate was used for all the binding kinetic experiments.

Binding assays were successively performed by a single-cycle kinetic (SCK) approach [55]. Four increasing concentrations of p28 peptide (analyte) in the range of 10–80 μM were sequentially injected over both the functionalized and the reference flow cell surfaces at a flow rate of 30 μl/min for 180 s followed by a 500 s dissociation time without intermediate regeneration. Binding assays also included three

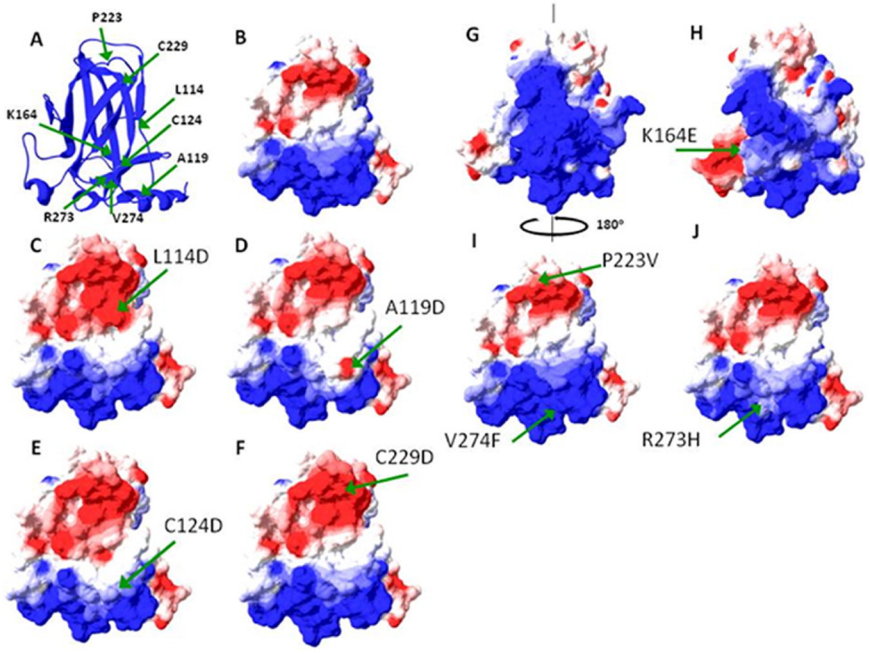

Fig. 2. (A) Ribbon-diagram of the wt p53 DBD. Arrows indicate the amino acid positions where mutations were introduced. The β-barrel structure of the p53 DBD orientated vertically. Molecular surfaces and electrostatic potentials of wt (B, G) and mut (C–F, H–J) p53 BD were calculated by DeepView (Swiss Institute of Bioinformatics). G, H: 180° rotated vertically. Arg, Lys, Glu and Asp were used as charged amino acids. Cationic and anionic areas are represented in blue and red, respectively.

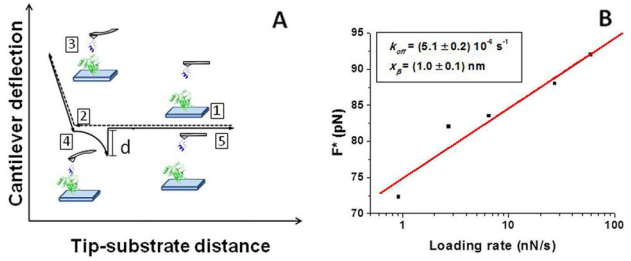

Fig. 3. (A) Schematic representation of a typical approach and retraction force-distance curve displaying a specific unbinding event between p28 anchored to the AFS tip and p53 DBD immobilized on a glass substrate. (B) Bell-Evans plot for the p28 interaction with the p53 DBD mutant K164E.

startup cycles using buffer to equilibrate the surface, as well a zero concentration cycle of analyte in order to have a blank response usable for double reference subtraction [56]. Analytical cycles were programmed by means of a wizard template and the entire analysis was completely automated.

To extract kinetic parameters from SPR data, experimental curves (sensorgrams) were double-reference subtracted. Specifically, the response collected over the functionalized surface was subtracted by the response from the reference surface to correct for bulk refractive index changes. Second, the response from running buffer injection was subtracted. Sensorgrams were then globally fitted using BiaEvaluation software 2.1 (GE Healthcare, BIOSciences AB, Sweden) to a 1:1 interaction model [56]. Goodness of the fit was evaluated based on visual inspection, on the χ^2 value (expected to be lower than 10) and on the residual plots.

3. Results and discussion

3.1. Molecular dynamic analysis of protein structure

We first investigated whether the binding and subsequent post-translation stabilization of p53^{mut} by p28 are dependent on the type of *e.g.* missense and location of the mutation within the p53 DBD. Docking analyses suggest that a significant number (~54%) of those residues on p53^{wt} predicted to bind p28 are within the L_1 and S_{7-8} loops of p53. Fig. 1A illustrates the identity and location of the predicted binding sites for p28 within the DBD of wild type p53 and the position of the amino acids selected for computational and site directed mutation. The amino-acids comprising the (28) predicted binding sites for p28 on p53wt are sequentially FLHSGTAVTCTYPALTPQWEGSDCTHRL. Seventeen of the predicted amino acids are located in the non-mutable L1 loop (10 aa) and the mutable S_7–S_8 loops (7 aa). Non-polar, hydrophobic amino acids within and outside the non-mutable L_1 loop as well as within the S_7 –S_8 loops were uniformly replaced with one with a strong anionic side chain (pKa ~ 3.7), the hydrophilic aspartate (D), to determine whether alterations in hydrophobicity might alter the predicted interaction between the p53 DBD and molecules such as p28. In addition, hydrophobic amino acids located within F113, G117 and outside P128, P142, the non-mutable L_1 loop predicted to bind p28, were computationally altered to aspartate for additional contrast. We generated hydrophilic to hydrophobic and hydrophilic to hydrophilic alterations at K120 within the L_1 loop (Fig. 1B) that is not predicted to interact with p28 and does not contact DNA [57] as a control for assessing the whether a loss in hydrophobicity was predictive of an altered binding. When a single hydrophobic to hydrophilic mutation was introduced in the L1 or S7–S8 loops of the p53 DBD, the predicted p28-binding sites on p53mut for F113D, L114D, G117D, V122D, C124D, P128D, P142D and C229 was KQLARCPHHRCDMNSSCMGRRCACRDTE. None of the predicted residues were located in the S7–S8 loops and only one residue (Lys120) was located in the L_1 loop. The amino acid composition of the predicted p28-binding sites on p53wt was 43% hydrophobic, 36% neutral and 21% hydrophilic, respectively. In contrast, those predicted for the p53 mutations were 25% hydrophobic, 36% neutral and 39% hydrophilic, a clear shift from hydrophobic to hydrophilic sites.

Computationally generated predictions of p28 binding suggest that 8/9 (~90%) p53 mutations that directly alter hydrophobicity within the L_1 and S_7–S_8 loops of the DBD of p53 or other motifs within the DBD or indirectly *e.g.* by introducing a large hydrophobic side chain (S241F) [26] can alter its ability to contact DNA [58]. These mutations also appear to consistently alter the predicted binding of p28 for p53 to more hydrophilic amino acids than observed for wild type p53. In contrast, the hydrophobic to hydrophilic substitution, A119D and negative control(s) did not alter the pattern observed on wild type p53. Fig. 2A presents a ribbon diagram illustrating the location of actual and site directed mutations as a function of secondary structure within the DBD of p53. Fig. 2B–J illustrates the contrast in electrostatic potential from wild type (Fig. 2B, G) generated by hydrophobic to hydrophilic substitutions within predicted binding sites for p28 (Fig. 2C–F) using the DeepView software package. Additional mutations within the DBD of solid tumor cells (Fig. 2H–J), previously modeled to assess potential binding, are also reanalyzed here with the DeepView software. Substitution of non-polar hydrophobic amino acids with the anionic (electrophilic) aspartic acid at positions 114 and 119 altered the surface charge from essentially neutral to anionic, while substitution of the special case (polar, hydrophobic) amino acid cysteine at positions 124 and 229 to aspartic acid slightly reduced the cationic (Fig. 2E) and increased the anionic surface charge (Fig. 2F) of the p53 DBD, respectively. The naturally occurring mutations at positions 164 (positive to negative, hydrophilic, Fig. 2H) altered the surrounding surface charge to anionic, while minimal changes to hydrophobicity, at 223 and 274 (Fig. 2I) did not alter surface charge. A slight reduction in positive charge and hydrophilicity in the naturally occurring mutation R273H (Fig. 2J) produced the expected slight reduction in surface charge.

We previously demonstrated that contact mutations that prevent p53 binding to DNA *e.g.* R273H (Fig. 2J) may, but do not necessarily, alter the binding motif for p28 on p53 [25]. This also appears true for either non-frameshift, internal deletions (Δ178–183, 25) or multiple missense mutations (P223L, V274F) (Fig. 2I) in cancer cells that essentially lie outside the L1 and S_7–S_8 loops, the major p53 DBD binding motifs for

Table 1
Kinetic parameters obtained by AFS for the interaction of p28 with WT-p53 DBD and site-directed mutants of the p53 DBD.

	AFS results				
Complex	k_{off} (s^{-1})	k_{on} (M^{-1} s^{-1})	K_D (M)	Unbinding frequency before blocking	Unbinding frequency after blocking
p29/WT-DBD	$(1.0 \pm 2.1) \cdot 10^{-5}$	$1.4 \cdot 10^{4}$	$0.7 \cdot 10^{-9}$	16.2%	8.8%
p29/L114D-DBD	$(3.0 \pm 4.0) \cdot 10^{-6}$	$4.8 \cdot 10^{3}$	$0.6 \cdot 10^{-9}$	11.2%	7.1%
p29/A119D-DBD	$(1.3 \pm 3.3) \cdot 10^{-3}$	$1.8 \cdot 10^{4}$	$0.7 \cdot 10^{-7}$	11.5%	6.9%
p29/C124D-DBD	No interaction	No interaction	No interaction	11.5%	10.6%
p29/C229D-DBD	No interaction	No interaction	No interaction	12.7%	10.8%

p28. These types of alterations allowed us to evaluate whether changes hydrophobicity within and outside the L_1 and S_{7-8} loops of the p53 DBD were responsible for or associated with potential changes in secondary structure that would alter the binding affinity for p28 or similar molecules.

3.2. AFS analyses of p28 binding to the p53 DBD

Force-distance curves were obtained by approaching/retracting, at a constant speed, the AFM tip functionalized with p28 to/from the glass substrate onto which $p53^{wt}$ DBD or mutated DBD molecules were covalently immobilized (Fig. 3A). At the beginning, the tip is far away from the surface, so there is no interaction between the two partners, and consequently no cantilever deflection is recorded (point 1). Successively, at the contact point (point 2), as due to the repulsive forces between molecules the cantilever begins to deflect. In the proximity of this point, a biorecognition process, eventually leading to the formation a specific complex between the two partners, may start to take place. Further approach of the tip results in an increasing overlap of the partners molecular orbitals whose repulsion produces a cantilever upward deflection. The approaching is stopped when a preset maximum force value is reached, to avoid damage of the proteins (point 3). The motion is then reversed and the cantilever begins to bend downwards due to the attractive force holding the complex (point 4). When the pulling force overcomes the biomolecular interacting force, the complex breaks and the cantilever jumps-off to a non-contact position (point 5), which is preceded by a nonlinear stretching of the molecular bonds of the PEG linker. Such a jump provides a measure of the unbinding force (called also rupture force) between the biomolecular partners. However, the approach of a functionalized tip toward a coated substrate, does not necessarily result into the formation of a specific complex. The force curves were thus analyzed by attributing a specific unbinding events to only those curves starting and ending at the zero-deflection line, and exhibiting a non-linear trend with the features of the PEG stretching [42,43].

The unbinding frequency (ratio between number of specific events over the total recorded curves) was calculated over all force-curves corresponding to specific unbinding events for each p29/DBD couple. Table 1 contrasts the binding of p28 (p29) to the DBD of $p53^{wt}$ and site directed mutants L114D, A119D, C124D and C229D. Although DeepView analysis (Fig. 2C, D) suggested that the L114D and A119D substitutions increased the anionic nature of the surface of the p53 DBD, docking analysis predicted that only the A119D substitution would allow binding of p28 to the correct amino acids. This was not the case. The unbinding frequency for the interaction of p28 with the site direct p53 DBD mutants L114D, A119D, C124D and C229D was ~12% compared to unbinding frequencies of 6–11% for the interaction between p28 and the naturally occurring p53 DBD mutants (K164E, R273H, P223L/V274F). Although quite low, the unbinding frequencies were consistent with the values found for other biological interactions [24,32] and could be ascribed to the lack of interaction between partners, presence of unfavorable binding geometries or steric hindrance. There was a significant reduction in the unbinding frequency after blocking only for the interaction between p28 and p53 DBD mutants L114D, A119D, K164E and P223L/V274F (Table 2). This suggests that p28 specifically interacts with these mutants even if steric hindrance or random immobilization significantly reduces the unbinding frequency. As predicted, neither the C124D nor C229D mutants specifically bound p28 as reflected by the absence of any reduction in the unbinding frequency after blocking for the interaction between p28 and C124D, C229D and R273H. (Table 1). Interestingly, a DBD with missense mutations at either K164 or P223 and V274 bound p28. The data directly reflect the relative activity of p28 to inhibit the proliferation of cancer cell lines bearing these mutations *in vitro* [25]. For each interaction, the k_{off} dissociation rates of the found specific interactions were then determined by plotting the most probable unbinding force (see the Materials and methods section for details) versus the natural logarithm of the loading rate, and then fitting data according to the Bell-Evans model [42,47,48] (see Fig. 3B); the obtained kinetic data being reported in Tables 1 and 2.

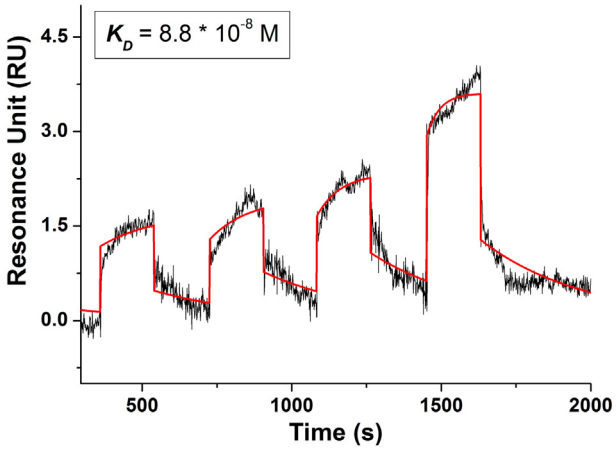

Fig. 4. Surface plasmon resonance sensorgram for the association and dissociation of p28 on wild type p53 DBD modified sensor chip surface (black line). The superimposed red line corresponds to the fit obtained by the 1:1 ligand model.

3.3. Surface Plasmon Resonance results

The SCK approach introduced by Karlsson and co workers [59] was used to study the interaction kinetics between wild type, single point and physiological p53 DBD mutants immobilized on the SPR sensor chip surface, and p28 in solution. Fig. 4 (black line) shows the SPR signal (RU) as a function of time for successive injections of increasing concentrations of p28 in the range of 10–80 μM on wild type p53 DBD functionalized sensor chip surface. As far as increasing concentrations of p28 are injected, a proportional increase of the SPR signal is observed that results from the specific interaction of an increasing amount of p28 with the immobilized p53 DBD. After 180 s of analyte injection, running buffer is fluxed over both the ligand and the reference surface and the SPR signal drops down as a consequence of the spontaneous dissociation of p28 and p53 DBD complexes. Similar trends were observed when increasing concentrations of p28 were fluxed over the K164E-DBD, or P223L/V274F-DBD functionalized sensor chip. No increase in signal was observed when the p28 interacted with the R273H-DBD functionalized sensor chip surface.

Table 2
Kinetic parameters obtained by AFS and SPR for the interaction of p28 with WT-p53 DBD and naturally occurring p53 DBD mutants.

	AFS results					SPR results
Complex	k_{off} (s^{-1})	k_{on} (M^{-1} s^{-1})	K_D (M)	Unbinding frequency before blocking	Unbinding frequency after blocking	K_D (M)
p29/K164E-DBD	$(5.1 \pm 0.2) \cdot 10^{-6}$	$6.1 \cdot 10^3$	$0.8 \cdot 10^{-9}$	10.5%	6.3%	$7.3 \cdot 10^{-8}$
p29/R273H-DBD	No interaction	No interaction	No interaction	8%	6.5%	No interaction
p29/P223L/V274F-DBD	(4.3 ± 2.2)	$3.2 \cdot 10^3$	$1.3 \cdot 10^{-3}$	6%	3%	$2.4 \cdot 10^{-4}$

Kinetic data provided by specific interactions, were analyzed in the framework of the Langmuir 1:1 binding model, which assumes a simple reversible bimolecular reaction between the ligand and the analyte [60] as described by the following equation:

$$L + A \underset{k_{off}}{\overset{k_{on}}{\rightleftarrows}} LA$$

where L is the ligand (the immobilized molecule), A is the analyte (molecule in solution); and k_{on} and k_{off} are the association and dissociation rates of the complex respectively; the corresponding K_D being given by k_{off}/k_{on}. Fig. 4, red line, shows the best fit obtained by the 1:1 binding model for the p28 (analyte) interaction with immobilized p53 DBD (ligand). Such a fit provided a k_{on} of $2.4 \cdot 10^2\ M^{-1}\ s^{-1}$, a k_{off} of $2.0 \cdot 10^{-5}\ s^{-1}$ and a K_D value of $8.8 \cdot 10^{-8}$ M, reported in Fig. 4, with a χ^2 value of 0.5. The K_D values obtained for the p28 interaction with physiological p53 DBD mutants, also reported in the last column of Table 2, qualitatively confirm the binding properties detected by AFS. The differences between the K_{Ds} values of about one-two orders of magnitude, provided by AFS and SPR, were similar to what has been previously obtained [61]. This can be certainly attributed to the peculiarities of the two experimental techniques, operating at level of single molecule in one case, AFS, and in bulk condition in the other, SPR, as well as to the different substrates and immobilization procedure used for p53 DBD immobilization.

3.4. Raman analysis of protein structure

We established an approach and baseline for determining the potential effect of mutations on secondary structure and their subsequent effects on p28 binding by analyzing the Raman spectra of the $p53^{wt}$ DBD. We confirmed that the Raman spectra of $p53^{wt}$ DBD identified the vibrational modes of the tyrosine (Tyr) aromatic ring at frequencies 643, 830, 850, 1174 and 1615 cm^{-1}, of phenylalanine (Phe) residues, at 620, 1006, 1030 and ~1605 cm^{-1}, tryptophan

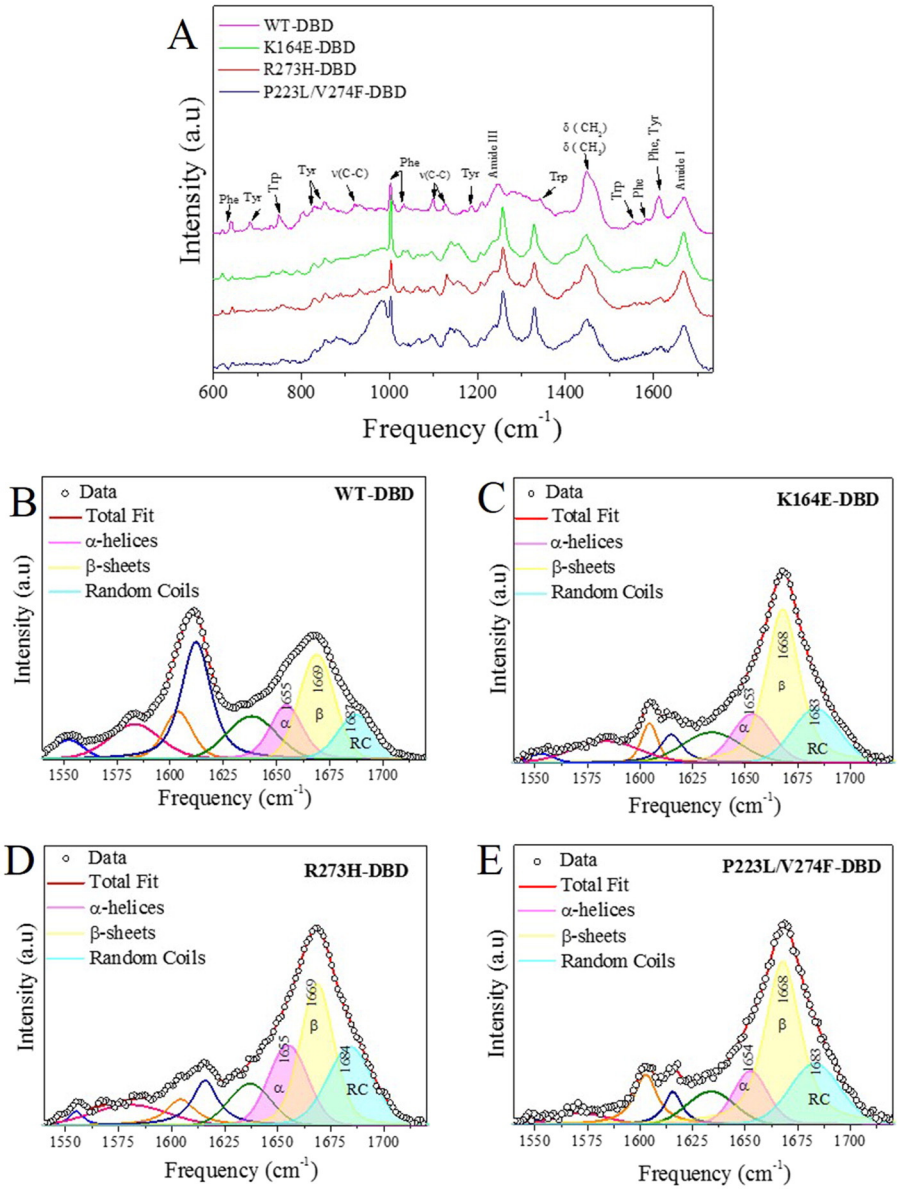

Fig. 5. (A) Raman spectra of WT-p53 DBD (magenta) and naturally occurring p53 DBD mutants (60 μM) in PBS in the 600–1725 cm^{-1} range. Principal vibrational modes are marked. (B, C, D, E). The corresponding Amide I Raman band (black circles) fitted using the three-component Voigt model (red line in each panels). The three bands associated with the main structural conformations of the protein are α-helix (magenta), β-sheet (yellow), and random coil (blue), respectively. Fitting results are summarized in Table 3 (excitation at 532 nm). Spectra were normalized to Amide I band.

(Trp), at 750, 1341, 1360 and 1550 cm^{-1}, the peaks at 950 cm^{-1} at ~1250 cm^{-1} represented C—C stretching and the Amide III band arising from an in-phase combination of N—H bending and C—N stretching with small contributions from the C═ O in-plane bending and C—C stretching with deformation of the CH_2—CH_3 bond resulting in a peak at 1447 cm^{-1}. Finally, an Amide I band, located within the spectral region 1620–1725 cm^{-1}, arises mainly from the C = O stretching vibration with minor contributions from out-of-phase C—N stretching, C—C—N deformation and an N—H in-plane bend (Fig. 5A) [62–65]. We focused our attention on the Amide I Raman band as it is strongly dependent on the secondary structure of each protein to provide detailed information on the overall structural conformation and distribution of multiple secondary structures following mutation of the p53 DBD [33].

The Amide I band of the $p53^{wt}$ DBD was fitted with three curves centered at 1650–1656, 1664–1670 and ~1680 cm^{-1} representing α-helix, β-sheet and random coil configurations, respectively [33,50,66]. Amide I band intensities were correlated with the fraction of each secondary structure, assuming that the Raman cross section of each conformation was identical. This assumption was validated by determining the ratio of the Amide I band with the tyrosine band at 1615 cm^{-1} an independent secondary structure in all samples [67]. The integrated area of the Amide I band relative to the Tyr ring band was similar (<20% under all conditions) validating the assumption. Curve fits for the $p53^{wt}$ DBD are shown in Fig. 5B with the corresponding fitting parameters recorded in Table 3.

The secondary structure of the $p53^{wt}$ DBD was 50% β-sheet, while the α-helix and random coil conformations contribute 27 and 23%, respectively to the total Amide I band area (Table 3) [35]. These data reflect the well characterized β-sandwich of the core domain and loop-sheet-helix nature of the DNA binding surface of p53.[1] In sum, the structural features of the $p53^{wt}$ DBD remain essentially constant or stable in the absence of the intrinsically disordered N- and C-terminal regions providing a baseline for analyses of mutational effects on secondary structure of the p53 DBD and their potential consequences on the binding of p28.

3.4.1. Effect of amino acid substitution on secondary structure

We compared the amount of α-helix, β-sheet and random coil of DBD^{wt} with those present in naturally occurring DBD mutants, K164E, R273H (DNA contact residue), a double mutation at P223L/V274F and directed single point mutations within the p53 DBD of cancer cells. The latter were designed to produce hydrophobic to hydrophilic changes in the normally non-mutable L_1 motif and within the S_{7-8} loop that bind p28, to provide insight as to how mutations that altered hydrophobicity might affect secondary structure and alter the binding of p28 or similar molecules.

Fig. 5A compares the Raman spectra of the three naturally occurring DBD mutants in PBS to the spectrum of wild-type DBD. Although the Raman spectra of the three mutants generally exhibited the same principal vibrational modes of DBD^{wt}, some spectral differences were observed. For example, the peak at 685 cm^{-1} was absent in all mutants. The region over 1124–1167 cm^{-1}, CH_2—CH_3 and Tyr vibrational modes show an evident deformation. The Amide III band at 1220–1298 cm^{-1} was significantly increased in two well defined and sharp peaks at 1252 and 1310 cm^{-1} in all three mutations, with the Amide I Raman band slightly narrower than in the DBD^{wt}.

The fitting curves of the Amide I Raman bands of the three naturally occurring mutant DBDs are shown in Fig. 5C–E, with the DBD^{wt} curve fit included for comparison (Fig. 5B); the corresponding fitting parameters are shown in Table 3. Deconvolution of the Amide I Raman band revealed that a β-sheet structure predominates in all the DBD mutants although the percentage appears to depend on the position of the mutation in the amino acid sequence. The results also suggest that mutations at K164E and P223L/V274F induce an increase in β-sheet content (59%) and a decrease in α-helical structure. The relative amount of random coil does not significantly change (~23%) from wt across the K164E and P223L/V274F mutations. In contrast, in PBS, the DNA-contact mutation (R273H) is associated with a significantly lower β-sheet (~42%), lower α-helix (~20%) and an increase in random coil content (~38%) suggesting an unwinding of that portion of the protein.

We next analyzed whether site-directed mutations within the L_1 and S_{7-8} loops of the p53 DBD (Fig. 1A, B) that resulted in a change in hydrophobicity altered conformation and p28 binding. The Raman spectra of the four site-directed mutations are shown in Fig. 6A. In general, each mutant exhibited a principal vibrational mode similar to the $p53^{wt}$ DBD. However, a slight shift in frequency of Tyr (830 and 850 cm^{-1}) and C—C stretching at 950 cm^{-1}, together with a deformation in the region identifying CH_2—CH_3 bonds (1400–1500 cm^{-1}) were observed in A119D and C124D spectra along with a narrowing of the width of the Amide I peak compared to the wild type DBD. In contrast, the Amide I was broader in the C229D substitution. There were no apparent spectral differences with respect to DBD^{wt} in the C124D spectrum. An analysis of the fitted Amide I region of the four site-directed mutants is shown in Fig. 6B–E. In PBS, the L114D and A119D directed mutations have a slightly elevated α-helix, a lower β-sheet and equal or slightly higher random coil content to that of the DBD^{wt} (Table 3). Substitution of the hydrophobic Leu114 and Ala119 with a hydrophilic (acidic) Asp residue within the highly conserved, non-mutable L_1 loop does not appear to significantly alter the secondary structure from the DBD^{wt}. However, when the slight shift in frequency of Tyr (830 and 850 cm^{-1}) and C—C stretching at 950 cm^{-1} and deformation in the region identifying CH_2—CH_3 bonds (1400–1500 cm^{-1}) observed in A119D are coupled with predictions that substitution of non-polar hydrophobic amino acids with the anionic (electrophilic) aspartic acid altered the surface charge from essentially neutral to anionic, it signals that these local changes contribute to the similar and slight decrease in affinity for p28 (Table 1) observed with these two mutations, respectively. In PBS, the C124D mutation (Fig. 6D) shows predominant α-helix (46%) and random coil (32%) regions while a β-sheet structure represents only 22% of the total. This is in sharp contrast to the DBD^{wt} pattern. The C229D mutation (Fig. 5E) also displays a significantly higher percentage of extended random coil conformation (65%) relative to DBD^{wt} (23%), with significantly less β-sheet (24%) and α-helix (11%) content (Table 3). Neither of these two mutations bound p28 (Table 1).

3.4.2. Effect of environmental changes on secondary structure

Deconvolution and curve fitting revealed that β-sheet content increased to 63% of the entire Amide I area of the DBD^{wt} in MeOH/PBS

Table 3
Fitting parameters of the Amide I band of WT-p53 DBD, naturally occurring and site-directed p53 DBD mutants in PBS. Standard deviations of the averaged area value are about ±10%, with $\chi^2 \leq 0.002$, for all curve fitting.

	Secondary structure			
Sample	α-Helix	β-Sheet	RC	
WT-DBD[a]	1655	1669	1687	Frequency (cm^{-1})
	27	50	23	Area %
K164E-DBD	1653	1668	1683	Frequency (cm^{-1})
	18	59	23	Area %
R273H-DBD	1655	1669	1684	Frequency (cm^{-1})
	20	42	38	Area %
P223L/V274F-DBD	1654	1668	1683	Frequency (cm^{-1})
	16	59	25	Area %
L114D-DBD	1653	1668	1684	Frequency (cm^{-1})
	27	48	25	Area %
A119D-DBD	1654	1669	1683	Frequency (cm^{-1})
	30	43	27	Area %
C124D-DBD	1654	1669	1683	Frequency (cm^{-1})
	46	22	32	Area %
C229D-DBD	1645	1660	1675	Frequency (cm^{-1})
	11	24	65	Area %

[a] Ref. [35].

solvent, significantly above the 50% content observed in PBS with a corresponding reduction in α-helix and RC content (Table 4). The altered polarity created by TFE/PBS increased α-helical content from 27% in DBD^{wt} in PBS to 51%, at the expense of β-sheet while the amount of random coil decreased to 18% together with a narrowing of the corresponding fit curve (data not shown) [35]. The observed substantial increase in β-sheet and α-helical content in MeOH and TFE, respectively, is in agreement with literature data on other proteins [33,35,68–73].

The results also suggest that the increase in α-helix essentially derives from β-sheet with a marginal contribution from random coil regions (Table 4). These observations generally confirm that environmental changes can modify secondary structure characterized by a narrowing of the Amide I band [33].

Further analysis of the curve fit data from Raman spectra showed only minimal changes in the main vibrational modes and spectral changes in Amide I bands of L114D and A119D from the DBD^{wt} in MeOH/PBS and TFE/PBS with peak widths similar to that in PBS (~47 cm^{-1} in both solvents). However, the width of the C124D and C229D Amide I peaks was narrower ~60 cm^{-1} in PBS to ~45 cm^{-1} in MeOH/PBS and ~51 cm^{-1} in TFE/PBS and ~78 cm^{-1} in PBS to ~46 cm^{-1} and ~53 cm^{-1}, in MeOH/PBS and TFE/PBS, respectively. The Amide I curve fit parameters following exposure of L114D to MeOH/PBS and TFE/PBS suggest that altering the hydrophobicity at L114 did not significantly reduce β-sheet content below that of DBD^{wt} (58 vs 63% [35]), but did increase the content of RC, suggesting that environmental alterations did not significantly alter the pattern of structural change from that of the DBD^{wt} under similar conditions. (Table 4). This observation supports the observation of a similar binding affinity of L114D for p28 (Table 1). However, exposure of A119D to MeOH reduced β-sheet content significantly below that of DBD^{wt} (49 vs 63%) that was accompanied by increases in α-helix and RC content. Preferential solvation with TFE, significantly increased β-sheet structure (52% vs 31%) from the DBD^{wt} at the expense of α-helix (39%) and RC (9%) content (Table 4). Overall, these results suggest that this mutation produced only marginal changes in β-sheet content and consequently, only a slight decrease in affinity for p28 (Table 1).

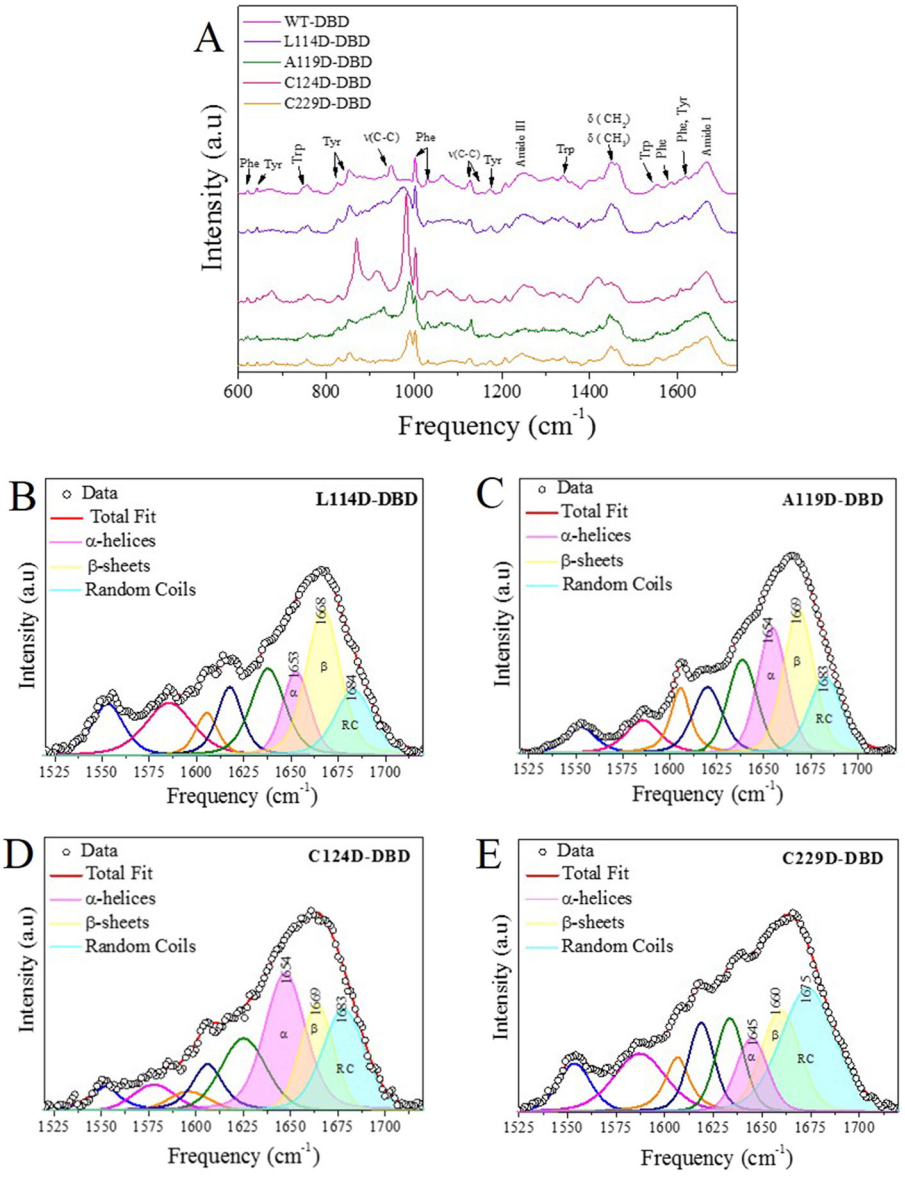

Fig. 6. (A) Raman spectra of WT-p53 DBD (magenta) and site-directed p53 DBD mutants (60 μM) in PBS in the 600–1725 cm^{-1} range. Principal vibrational modes are marked. (B, C, D, E). The corresponding Amide I Raman band (black circles) fitted using the three-component Voigt model (red line in each panels). The three bands associated with the main structural conformations of the protein are α-helix (magenta), β-sheet (yellow), and random coil (blue), respectively. Fitting results are summarized in Table 3 (excitation at 532 nm). Spectra were normalized to Amide I band.

Table 4
Fitting parameters of the Amide I band of WT-p53 DBD, naturally occurring and site-directed p53 DBD mutants in MeOH/PBS and TFE/PBS solvents. Standard deviations of the averaged area value are about ±10%, with $\chi^2 \leq 0.002$, for all curve fitting.

Solvent	MeOH/PBS			TFE/PBS			
	Secondary structure			Secondary structure			
Sample	α-Helix	β-Sheet	RC	α-Helix	β-Sheet	RC	
WT-DBD[a]	1654	1670	1688	1655	1671	1687	Frequency (cm^{-1})
	20	63	17	51	31	18	Area %
K164E-DBD	1654	1669	1688	1662	1672	1687	Frequency (cm^{-1})
	17	65	18	45	35	20	Area %
R273H-DBD	1655	1669	1686	1661	1670	1687	Frequency (cm^{-1})
	23	51	26	48	29	23	Area %
P223L/V274F-DBD	1654	1668	1684	1664	1671	1687	Frequency (cm^{-1})
	19	57	24	49	36	15	Area %
L114D-DBD	1655	1668	1685	1649	1669	1688	Frequency (cm^{-1})
	17	58	25	46	35	19	Area %
A119D-DBD	1656	1668	1682	1657	1671	1688	Frequency (cm^{-1})
	26	49	25	39	52	9	Area %
C124D-DBD	1653	1668	1682	1657	1672	1689	Frequency (cm^{-1})
	23	54	23	53	33	14	Area %
C229D-DBD	1653	1667	1683	1654	1667	1680	Frequency (cm^{-1})
	17	53	30	46	37	17	Area %

[a] Ref. [35].

In contrast to the significant reduction in β-sheet content from DBD^{wt} observed with C124D in PBS (22 vs 50%), exposure of C124D to MeOH only decreased β-sheet content of about 14% accompanied by slight increases in α-helix and random coil compared to DBD^{wt}. The marginal increases in α-helix and β-sheet content of C124D relative to DBD^{wt} in the presence of TFE suggest that the loss of β-sheet under physiologic conditions did not result in a loss of overall flexibility in the mutant DBD, but did eliminate the ability to bind p28. A similar solvent effect with C229D, loss of β-sheet (15%) and increase in RC (43%) content with MeOH, reversed after exposure to TFE (Table 4) suggests that the mutation results in a highly disordered DBD with a significant increase in unstructured regions (RC), that while incapable of binding p28, do remain able to respond to changes in polarity. This in turn suggests that mutations within this region of the p53 DBD are potentially pharmacologically resolvable.

4. Conclusions

The p53 DNA binding or core domain of p53 folds into an immunoglobulin-like β-sandwich (two anti-parallel β-sheets) with a DNA binding surface that binds to the major and minor grooves of sequence-specific (target) DNA at promoter regions and initiates gene transcription. The major groove binding surface is formed by the L_1 loop and a short helix H2 (residues P278–E287). The minor groove binding surface is formed by two loops, L_2 (residues K164–C176, C182–L194) and L_3 (residues M237–P250, 57). L_1 is the most dynamic loop among L_1, L_2 and L_3. The high flexibility of L_1 arises because residues H115, S116, and G117 of L_1 have very little interaction with the bulk protein except for a hydrogen bond between S116 and C124 of L_1, and S_2 interface [74].

Intrinsically disordered regions, terminal tails, and flexible linkers are abundant in DNA-binding proteins and play a crucial role by increasing the affinity and specificity of DNA binding [75]. The modular domain structure of p53 consists of folded DNA-binding and tetramerization domains, flanked by intrinsically disordered regions at both the amino- and carboxy-termini. The concerted action of folded and intrinsically disordered domains of the highly dynamic p53 protein provides binding promiscuity and specificity, allowing p53 to process a myriad of cellular signals to maintain the integrity of the human genome [76]. The secondary structural characteristics between a full-length p53 and its DBD identified by Raman spectroscopy differ significantly only in the increase of random coil relative to β-sheet, respectively [48], suggesting that any mutations within the DBD that alter its secondary structure and affect binding to DNA are likely to be causal and essentially not subject to significant modification by its intrinsically disordered regions. A similar argument would appear to be valid for the binding of p28 to its predicted motifs within the DBD.

p28, a linear, 28 amino acid, amphipathic peptide derived from the copper containing redox protein azurin, binds with high affinity to the DBD of p53 [24] without altering its conformation and post-translationally activates p53 [25,26]. Molecular dynamic analyses predict that the majority of p28 binding sites are within the non-mutated L_1 loop (a.a 112–124) [29] and a mutable region *e.g.* (Y220C, P223L) within the S_{7-8} loops (aa 214–236) of the DBD [23] and bind p28 through hydrophobic interaction. We speculated that mutations in the L_1 and S_7–S_8 loops directed at amino acids predicted to bind p28 might compromise local secondary structure sufficiently to alter the affinity for p28 and confirm the predicted regional binding motifs. The *hotspot* Y220C mutation in the latter loop unfolds p53 > 80% [77]. We show here that the effect of altering side chain charge and hydrophobicity on p28 binding is due to local changes in secondary structure within the L_1 and S_{7-8} loops of the p53 DBD, rather than extensive unfolding of the molecule.

Molecular dynamic simulations and docking analyses predict that altering the hydrophobicity of selected amino acids within the L_1 and S_7–S_8 loops can potentially alter, and even increase the number of sites binding p53, while maintaining or reversing the hydrophilicity of the nonbinding K120 does not (Fig. 1). However, the L114D mutation in L_1, predicted to alter the binding site of p28, did not significantly alter the affinity (K_D) of the mutant for p28, while the A119D mutation lowered it (Table 1) in the presence of significant local changes in electrostatic potential (Fig. 2C, D). This suggests that a mutation at L114 is either not critical to p28 binding or that p28 binds to an alternative motif within the DBD, at a similar affinity suggesting some degree in the flexibility of p28 binding within. Our prediction suggests the latter. As Leu is the most hydrophobic residue in the series L114, A119, C124 and C229 [78] a significant reduction in hydrophobicity at position 114 does not appear critical for p28 binding. However, if binding is to an alternative site, it may be reflected by the increase in random coil content of this mutant relative to the wt DBD in the presence of MeOH. As predicted the A119D mutation continued to bind p28, albeit at a slightly lower affinity (Table 1). Here again, the loss of β-sheet content in MeOH and increase in RC relative to DBD^{wt} and L114D are observed (Tables 3, 4). The relative content of α-helix and β-sheet of these directed L_1 mutations mirrors that of the natural mutations K164E and P223L/V274F across solvents (Table 4) suggesting that

missense mutations cause similar types of local disruptions in secondary structure across the DBD, irrespective of whether the mutation produces a change in hydrophobicity. The significant decrease in β-sheet and increase in random coil associated with the R273H mutation (Table 4) and inability to respond to MeOH with an increase in β-sheet are reflected in the absence of predicted and actual (Table 2) binding of p28 to p53.

The significant loss of β-sheet in C124D and C229D mutations and higher content of an extended random coil conformation relative to DBD^{wt} provide further evidence that local changes in hydrophobicity can significantly alter DBD scaffold organization. Modeling substitution of the special case (polar, hydrophobic) amino acid cysteine [79] at positions 124 and 229 to aspartic acid showed a reduced cationic (Fig. 2E) and increased anionic surface charge (Fig. 2F) of the p53 DBD, respectively. The C124D mutation is at the C-terminus of the L_1 loop at the initiation of a β-sheet (S_2) (Fig. 1), while C229D is central within the S_{7-8} loop. This may provide an explanation of why we observed a significant reduction in β-sheet content relative to DBD^{wt} and L_1 mutations. As the overall NMR structure of p53 core domain is a β-sandwich, composed of two antiparallel β-sheets with a small β-hairpin (124–135) in contact with the second β-sheet, closing the access to the hydrophobic core, altering hydrophobicity and charge of the C-terminus of the L_1 loop or the β-hairpin would appear to strongly reduce p28 binding (Table 1). A similar case could be made for the S_{7-8} loop.

Raman spectroscopy coupled with AFS and SPR analyses, provided an alternative approach to define how local alterations in secondary structure affected the binding of p28 to the DBD of p53. The combination of molecular dynamic modeling with docking analysis, atomic force and Raman spectroscopy and a suitable fitting procedure allowed us to conclusively demonstrate that p28 does bind to the DBD of p53 and confirm predictions of those binding motifs. A solvent perturbation strategy detailed the ensemble of conformations adopting different secondary structures within the DBD in response to missense mutations and showed how they are dependent on the position of the mutation along the protein chain. These observations provide additional evidence on how p28 is active in initial clinical trials in patients with a variety of advanced, $p53^{wt,mut}$ positive tumors [80,81]. Additional efforts to define how p28 and similar peptides/proteins stabilize wt and mutated p53 will no doubt improve the performance of this type of agent.

Acknowledgements

This work was partly supported by a Grant from the Italian Association for Cancer Research (AIRC No. IG 15866) and by a PRIN-MIUR 2012 Project (No. 2012NRRP5J).

References

[1] Y. Cho, S. Gorina, P.D. Jeffrey, N.P. Pavletich, Crystal structure of a p53 tumor suppressor-DNA complex: understanding tumorigenic mutations, Science 265 (1994) 346–355, http://dx.doi.org/10.1126/science.8023157.
[2] S. Bell, C. Klein, L. Mueller, S. Hansen, J. Buchner, P53 contains large unstructured regions in its native state, J. Mol. Biol. 322 (2002) 917–927, http://dx.doi.org/10.1016/S0022-2836(02)00848-3.
[3] J.M.P. Cañadillas, H. Tidow, S.M.V. Freund, T.J. Rutherford, H.C. Ang, A.R. Fersht, Solution structure of p53 core domain: structural basis for its instability, Proc. Natl. Acad. Sci. U. S. A. 103 (2006) 2109–2114, http://dx.doi.org/10.1073/pnas.0510941103.
[4] M.M. Babu, R. van der Lee, N.S. de Groot, J. Gsponer, Intrinsically disordered proteins: regulation and disease, Curr. Opin. Struct. Biol. 21 (2011) 432–440, http://dx.doi.org/10.1016/j.sbi.2011.03.011.
[5] J.D. Forman-Kay, T. Mittag, From sequence and forces to structure, function, and evolution of intrinsically disordered proteins, Structure 21 (2013) 1492–1499, http://dx.doi.org/10.1016/j.str.2013.08.001.
[6] L. Collavin, A. Lunardi, G. Del Sal, p53-family proteins and their regulators: hubs and spokes in tumor suppression, Cell Death Differ. 17 (2010) 901–911, http://dx.doi.org/10.1038/cdd.2010.35.
[7] M. Olivier, R. Eeles, M. Hollstein, M.A. Khan, C.C. Harris, P. Hainaut, The IARC TP53 database: new online mutation analysis and recommendations to users, Hum. Mutat. 19 (2002) 607–614, http://dx.doi.org/10.1002/humu.10081.
[8] A.C. Joerger, H.C. Ang, D.B. Veprintsev, C.M. Blair, A.R. Fersht, Structures of p53 cancer mutants and mechanism of rescue by second-site suppressor mutations, J. Biol. Chem. 280 (2005) 16030–16037, http://dx.doi.org/10.1074/jbc.M500179200.
[9] E.M. Alexandrova, A.R. Yallowitz, D. Li, S. Xu, R. Schulz, D.A. Proia, G. Lozano, M. Dobbelstein, U.M. Moll, Improving survival by exploiting tumour dependence on stabilized mutant p53 for treatment, Nature 523 (2015) 352–356, http://dx.doi.org/10.1038/nature14430\rnature14430 (pii).
[10] R. Brosh, V. Rotter, When mutants gain new powers: news from the mutant p53 field, Nat. Rev. Cancer (2009)http://dx.doi.org/10.1038/nrc2693.
[11] M. Oren, V. Rotter, Mutant p53 gain-of-function in cancer, Cold Spring Harb. Perspect. Biol. 2 (2010)http://dx.doi.org/10.1101/cshperspect.a001107.
[12] D. Menendez, A. Inga, M.A. Resnick, Potentiating the p53 network, Discov. Med. 10 (2010) 94–100.
[13] H. Viadiu, G. Fronza, A. Inga, Structural Studies on Mechanisms to Activate Mutant p53, 2014 119–132, http://dx.doi.org/10.1007/978-94-017-9211-0_7.
[14] W.A. Freed-Pastor, C. Prives, Mutant p53: one name, many proteins, Genes Dev. 26 (2012) 1268–1286, http://dx.doi.org/10.1101/gad.190678.112.
[15] L. Römer, C. Klein, A. Dehner, H. Kessler, J. Buchner, p53—a natural cancer killer: structural insights and therapeutic concepts, Angew. Chem. Int. Ed. 45 (2006) 6440–6460, http://dx.doi.org/10.1002/anie.200600611.
[16] M. Aggarwal, R. Saxena, E. Sinclair, Y. Fu, A. Jacobs, M. Dyba, X. Wang, I. Cruz, D. Berry, B. Kallakury, S.C. Mueller, S.D. Agostino, G. Blandino, M.L. Avantaggiati, F.-L. Chung, Reactivation of mutant p53 by a dietary-related compound phenethyl isothiocyanate inhibits tumor growth, Cell Death Differ. 23 (2016) 1615–1627, http://dx.doi.org/10.1038/cdd.2016.48.
[17] P. Tal, S. Eizenberger, E. Cohen, N. Goldfinger, S. Pietrokovski, M. Oren, V. Rotter, Cancer therapeutic approach based on conformational stabilization of mutant p53 protein by small peptides, Oncotarget 7 (2016) 11817–11837, http://dx.doi.org/10.18632/oncotarget.7857.
[18] A. Parrales, T. Iwakuma, Targeting oncogenic mutant p53 for cancer therapy, Front. Oncol. 5 (2015) 288, http://dx.doi.org/10.3389/fonc.2015.00288.
[19] D. Apiyo, P. Wittung-Stafshede, Unique complex between bacterial azurin and tumor-suppressor protein p53, Biochem. Biophys. Res. Commun. 332 (2005) 965–968, http://dx.doi.org/10.1016/j.bbrc.2005.05.038.
[20] A.R. Bizzarri, S. Di Agostino, L. Andolfi, S. Cannistraro, A combined atomic force microscopy imaging and docking study to investigate the complex between p53 DNA binding domain and azurin, J. Mol. Recognit. 22 (2009) 506–515, http://dx.doi.org/10.1002/jmr.975.
[21] V. De Grandis, A.R. Bizzarri, S. Cannistraro, Docking study and free energy simulation of the complex between p53 DNA-binding domain and azurin., J. Mol. Recognit. 20 (n.d.) 215–26. doi:10.1002/jmr.840.
[22] M. Taranta, A.R. Bizzarri, S. Cannistraro, Probing the interaction between p53 and the bacterial protein azurin by single molecule force spectroscopy, J. Mol. Recognit. 21 (2008) 63–70, http://dx.doi.org/10.1002/jmr.869.
[23] M. Taranta, A.R. Bizzarri, S. Cannistraro, Modeling the interaction between the N-terminal domain of the tumor suppressor p53 and azurin, J. Mol. Recognit. 22 (2009) 215–222, http://dx.doi.org/10.1002/jmr.934.
[24] A.R. Bizzarri, S. Santini, E. Coppari, M. Bucciantini, S. Di Agostino, T. Yamada, C.W. Beattie, S. Cannistraro, Interaction of an anticancer peptide fragment of azurin with p53 and its isolated domains studied by atomic force spectroscopy, Int. J. Nanomedicine 6 (2011) 3011–3019, http://dx.doi.org/10.2147/IJN.S26155.
[25] T. Yamada, K. Christov, A. Shilkaitis, L. Bratescu, A. Green, S. Santini, A.R. Bizzarri, S. Cannistraro, T.K.D. Gupta, C.W. Beattie, p28, a first in class peptide inhibitor of cop1 binding to p53, Br. J. Cancer 108 (2013) 2495–2504, http://dx.doi.org/10.1038/bjc.2013.266.
[26] T. Yamada, T.K. Das Gupta, C.W. Beattie, P28, an anionic cell-penetrating peptide, increases the activity of wild type and mutated p53 without altering its conformation, Mol. Pharm. 10 (2013) 3375–3383, http://dx.doi.org/10.1021/mp400221r.
[27] A. Friedler, L.O. Hansson, D.B. Veprintsev, S.M.V. Freund, T.M. Rippin, P.V. Nikolova, M.R. Proctor, S. Rudiger, A.R. Fersht, A peptide that binds and stabilizes p53 core domain: chaperone strategy for rescue of oncogenic mutants, Proc. Natl. Acad. Sci. 99 (2002) 937–942, http://dx.doi.org/10.1073/pnas.241629998.
[28] A. Inga, M.A. Resnick, Novel human p53 mutations that are toxic to yeast can enhance transactivation of specific promoters and reactivate tumor p53 mutants, Oncogene 20 (2001) 3409–3419, http://dx.doi.org/10.1038/sj.onc.1204457.
[29] A. Zupnick, C. Prives, Mutational analysis of the p53 core domain L1 loop, J. Biol. Chem. 281 (2006) 20464–20473, http://dx.doi.org/10.1074/jbc.M603387200.
[30] T. Yamada, R.R. Mehta, F. Lekmine, K. Christov, M.L. King, D. Majumdar, A. Shilkaitis, A. Green, L. Bratescu, C.W. Beattie, T.K. Das Gupta, A peptide fragment of azurin induces a p53-mediated cell cycle arrest in human breast cancer cells, Mol. Cancer Ther. 8 (2009) 2947–2958, http://dx.doi.org/10.1158/1535-7163.MCT-09-0444.
[31] E. Coppari, T. Yamada, A.R. Bizzarri, C.W. Beattie, S. Cannistraro, A nanotechnological, molecular-modeling, and immunological approach to study the interaction of the anti-tumorigenic peptide p28 with the p53 family of proteins, Int. J. Nanomedicine 9 (2014) 1799–1813, http://dx.doi.org/10.2147/IJN.S58465.
[32] S. Santini, A.R. Bizzarri, S. Cannistraro, Modelling the interaction between the p53 DNA-binding domain and the p28 peptide fragment of azurin, J. Mol. Recognit. 24 (2011) 1043–1055, http://dx.doi.org/10.1002/jmr.1153.
[33] N.C. Maiti, M.M. Apetri, M.G. Zagorski, P.R. Carey, V.E. Anderson, Raman spectroscopic characterization of secondary structure in natively unfolded proteins: alpha-synuclein, J. Am. Chem. Soc. 126 (2004) 2399–2408, http://dx.doi.org/10.1021/ja0356176.
[34] T. Yamada, S. Signorelli, S. Cannistraro, C.W. Beattie, A.R. Bizzarri, Chirality switching within an anionic cell-penetrating peptide inhibits translocation without affecting preferential entry, Mol. Pharm. 12 (2015) 140–149, http://dx.doi.org/10.1021/mp500495u.

[35] S. Signorelli, S. Cannistraro, A.R. Bizzarri, Structural characterization of the intrinsically disordered protein p53 using Raman spectroscopy, Appl. Spectrosc. (2016) 1–10, http://dx.doi.org/10.1177/0003702816651891.

[36] K. Xiong, M.C. Zwier, N.S. Myshakina, V.M. Burger, S.A. Asher, L.T. Chong, Direct observations of conformational distributions of intrinsically disordered p53 peptides using UV Raman and explicit solvent simulations, J. Phys. Chem. A 115 (2011) 9520–9527, http://dx.doi.org/10.1021/jp112235d.

[37] M.A. Cooper, Label-free Screening of Bio-molecular Interactions, 2003 834–842, http://dx.doi.org/10.1007/s00216-003-2111-y.

[38] M. Fioroni, M.D. Diaz, K. Burger, S. Berger, Solvation phenomena of a tetrapeptide in water/trifluoroethanol and water/ethanol mixtures: a diffusion NMR, intermolecular NOE, and molecular dynamics study, J. Am. Chem. Soc. 124 (2002) 7737–7744, http://dx.doi.org/10.1021/ja0259335.

[39] V. Vacic, P.R.L. Markwick, C.J. Oldfield, X. Zhao, C. Haynes, V.N. Uversky, L.M. Iakoucheva, Disease-associated mutations disrupt functionally important regions of intrinsic protein disorder, PLoS Comput. Biol. 8 (2012), e1002709. http://dx.doi.org/10.1371/journal.pcbi.1002709.

[40] J.L. Hutter, J. Bechhoefer, Calibration of atomic-force microscope tips, Rev. Sci. Instrum. 64 (1993) 1868, http://dx.doi.org/10.1063/1.1143970.

[41] C. Friedsam, A.K. Wehle, F. Kuehner, H.E. Gaub, Dynamic single-molecule force spectroscopy: bond rupture analysis with variable spacer length, J. Phys. Condens. Matter 15 (2003) S1709–S1723, http://dx.doi.org/10.1088/0953-8984/15/18/305.

[42] A.R. Bizzarri, S. Cannistraro, The application of atomic force spectroscopy to the study of biological complexes undergoing a biorecognition process, Chem. Soc. Rev. 39 (2010) 734–749, http://dx.doi.org/10.1039/b811426a.

[43] A.R. Bizzarri, S. Cannistraro, Atomic force spectroscopy in biological complex formation: strategies and perspectives, J. Phys. Chem. B 113 (2009) 16449–16464, http://dx.doi.org/10.1021/jp902421r.

[44] T.A. Sulchek, R.W. Friddle, K. Langry, E.Y. Lau, H. Albrecht, T.V. Ratto, S.J. DeNardo, M.E. Colvin, A. Noy, Dynamic force spectroscopy of parallel individual Mucin1-antibody bonds, Proc. Natl. Acad. Sci. U. S. A. 102 (2005) 16638–16643, http://dx.doi.org/10.1073/pnas.0505208102.

[45] W. Baumgartner, P. Hinterdorfer, W. Ness, A. Raab, D. Vestweber, H. Schindler, D. Drenckhahn, Cadherin interaction probed by atomic force microscopy, Proc. Natl. Acad. Sci. U. S. A. 97 (2000) 4005–4010, http://dx.doi.org/10.1073/pnas.070052697.

[46] T.V. Ratto, K.C. Langry, R.E. Rudd, R.L. Balhorn, M.J. Allen, McElfresh, force spectroscopy of the double-tethered concanavalin-a mannose bond, Biophys. J. 86 (2004) 2430–2437, http://dx.doi.org/10.1016/S0006-3495(04)74299-X.

[47] G.I. Bell, Models for the specific adhesion of cells to cells, Science 200 (1978) 618–627.

[48] E. Evans, K. Ritchie, Dynamic strength of molecular adhesion bonds, Biophys. J. 72 (1997) 1541–1555, http://dx.doi.org/10.1016/S0006-3495(97)78802-7.

[49] P. Hinterdorfer, W. Baumgartner, H.J. Gruber, K. Schilcher, H. Schindler, Detection and localization of individual antibody-antigen recognition events by atomic force microscopy, Proc. Natl. Acad. Sci. U. S. A. 93 (1996) 3477–3481.

[50] A. Won, S. Pripotnev, A. Ruscito, A. Ianoul, Effect of point mutations on the secondary structure and membrane interaction of antimicrobial peptide anoplin, J. Phys. Chem. B 115 (2011) 2371–2379, http://dx.doi.org/10.1021/jp108343g.

[51] D. Kozakov, D.R. Hall, D. Beglov, R. Brenke, S.R. Comeau, Y. Shen, K. Li, J. Zheng, P. Vakili, I.C. Paschalidis, S. Vajda, Achieving reliability and high accuracy in automated protein docking: Cluspro, PIPER, SDU, and stability analysis in CAPRI rounds 13–19, Proteins Struct. Funct. Bioinforma. 78 (2010) 3124–3130, http://dx.doi.org/10.1002/prot.22835.

[52] C. Zhang, G. Vasmatzis, J.L. Cornette, C. DeLisi, Determination of atomic desolvation energies from the structures of crystallized proteins, J. Mol. Biol. 267 (1997) 707–726, http://dx.doi.org/10.1006/jmbi.1996.0859.

[53] C.J. Camacho, S.R. Kimura, C. DeLisi, S. Vajda, Kinetics of desolvation-mediated protein-protein binding, Biophys. J. 78 (2000) 1094–1105, http://dx.doi.org/10.1016/S0006-3495(00)76668-9.

[54] C. Reynolds, D. Damerell, S. Jones, ProtorP: a protein-protein interaction analysis server, Bioinformatics 25 (2009) 413–414, http://dx.doi.org/10.1093/bioinformatics/btn584.

[55] S. Santini, A.R. Bizzarri, T. Yamada, C.W. Beattie, S. Cannistraro, Binding of azurin to cytochrome *c* 551 as investigated by surface plasmon resonance and fluorescence, J. Mol. Recognit. 27 (2014) 124–130, http://dx.doi.org/10.1002/jmr.2346.

[56] T.A. Morton, D.G. Myszka, Kinetic analysis of macromolecular interactions using surface plasmon resonance biosensors, Methods Enzymol. 295 (1998) 268–294.

[57] S. Lukman, D.P. Lane, C.S. Verma, Mapping the structural and dynamical features of multiple p53 DNA binding domains: insights into loop 1 intrinsic dynamics, PLoS One 8 (2013) 1–19, http://dx.doi.org/10.1371/journal.pone.0080221.

[58] M. Olivier, M. Hollstein, P. Hainaut, TP53 mutations in human cancers: origins, consequences, and clinical use, Cold Spring Harb. Perspect. Biol. 2 (2010) a001008, http://dx.doi.org/10.1101/cshperspect.a001008.

[59] R. Karlsson, P.S. Katsamba, H. Nordin, E. Pol, D.G. Myszka, Analyzing a kinetic titration series using affinity biosensors, Anal. Biochem. 349 (2006) 136–147, http://dx.doi.org/10.1016/j.ab.2005.09.034.

[60] D.J. O'Shannessy, M. Brigham-Burke, K.K. Soneson, P. Hensley, I. Brooks, Determination of rate and equilibrium binding constants for macromolecular interactions using surface plasmon resonance: use of nonlinear least squares analysis methods, Anal. Biochem. 212 (1993) 457–468.

[61] S. Santini, S. Di Agostino, E. Coppari, A.R. Bizzarri, G. Blandino, S. Cannistraro, Interaction of mutant p53 with p73: a surface plasmon resonance and atomic force spectroscopy study, Biochim. Biophys. Acta 1840 (2014) 1958–1964, http://dx.doi.org/10.1016/j.bbagen.2014.02.014.

[62] S. Krimm, J. Bandekar, Vibrational spectroscopy and conformation of peptides, polypeptides, and proteins, Adv. Protein Chem. 38 (1986) 181–364, http://dx.doi.org/10.1016/S0065-3233(08)60528-8.

[63] L. Laporte, J. Stultz, G.J. Thomas, Solution conformations and interactions of α and β subunits of the *Oxytricha nova* telomere binding protein: investigation by Raman spectroscopy†, Biochemistry 36 (1997) 8053–8059, http://dx.doi.org/10.1021/bi970283g.

[64] T. Miura, G.J. Thomas, Raman Spectroscopy of Proteins and Their Assemblies, Springer, US, 1995 55–99, http://dx.doi.org/10.1007/978-1-4899-1727-0_3.

[65] P.R. Carey, Biochemical Applications of Raman and Resonance Raman Spectroscopies, Academic Press, 1982.

[66] R. Tuma, Raman spectroscopy of proteins: from peptides to large assemblies, J. Raman Spectrosc. 36 (2005) 307–319, http://dx.doi.org/10.1002/jrs.1323.

[67] S.U. Sane, S.M. Cramer, T.M. Przybycien, A holistic approach to protein secondary structure characterization using amide I band Raman spectroscopy, Anal. Biochem. 272 (1999) 255–272, http://dx.doi.org/10.1006/abio.1999.4034.

[68] L.A. Munishkina, C. Phelan, V.N. Uversky, A.L. Fink, Conformational behavior and aggregation of α-synuclein in organic solvents: modeling the effects of membranes†, Biochemistry 42 (2003) 2720–2730, http://dx.doi.org/10.1021/bi027166s.

[69] M.D. Díaz, M. Fioroni, K. Burger, S. Berger, Evidence of complete hydrophobic coating of bombesin by trifluoroethanol in aqueous solution: an NMR spectroscopic and molecular dynamics study, Chemistry 8 (2002) 1663–1669.

[70] S. Fatima, B. Ahmad, R.H. Khan, Fluoroalcohols induced unfolding of Succinylated Con A: native like β-structure in partially folded intermediate and α-helix in molten globule like state, Arch. Biochem. Biophys. 454 (2006) 170–180, http://dx.doi.org/10.1016/j.abb.2006.08.014.

[71] K. Gast, D. Zirwer, M. Müller-Frohne, G. Damaschun, Trifluoroethanol-induced conformational transitions of proteins: insights gained from the differences between α-lactalbumin and ribonuclease A, Protein Sci. 8 (2008) 625–634, http://dx.doi.org/10.1110/ps.8.3.625.

[72] P. Gupta, R.H. Khan, M. Saleemuddin, Trifluoroethanol-induced "molten globule"; state in stem bromelain, Arch. Biochem. Biophys. 413 (2003) 199–206.

[73] D. Roccatano, M. Fioroni, M. Zacharias, G. Colombo, Effect of hexafluoroisopropanol alcohol on the structure of melittin: a molecular dynamics simulation study, Protein Sci. 14 (2005) 2582–2589, http://dx.doi.org/10.1110/ps.051426605.

[74] Y. Pan, B. Ma, R.B. Venkataraghavan, A.J. Levine, R. Nussinov, In the quest for stable rescuing mutants of p53: computational mutagenesis of flexible loop L1†, Biochemistry 44 (2005) 1423–1432, http://dx.doi.org/10.1021/bi047845y.

[75] D. Vuzman, Y. Levy, Intrinsically disordered regions as affinity tuners in protein–DNA interactions, Mol. BioSyst. 8 (2012) 47–57, http://dx.doi.org/10.1039/C1MB05273J.

[76] A.C. Joerger, A.R. Fersht, The tumor suppressor p53: from structures to drug discovery, Cold Spring Harb. Perspect. Biol. 2 (2010) a000919, http://dx.doi.org/10.1101/cshperspect.a000919.

[77] A.C. Joerger, H.C. Ang, A.R. Fersht, Structural basis for understanding oncogenic p53 mutations and designing rescue drugs, Proc. Natl. Acad. Sci. 103 (2006) 15056–15061, http://dx.doi.org/10.1073/pnas.0607286103.

[78] J. Kyte, R.F. Doolittle, A simple method for displaying the hydropathic character of a protein, J. Mol. Biol. 157 (1982) 105–132.

[79] J.L. Cornette, K.B. Cease, H. Margalit, J.L. Spouge, J.A. Berzofsky, C. DeLisi, Hydrophobicity scales and computational techniques for detecting amphipathic structures in proteins, J. Mol. Biol. 195 (1987) 659–685.

[80] R.R. Lulla, S. Goldman, T. Yamada, C.W. Beattie, L. Bressler, M. Pacini, I.F. Pollack, P.G. Fisher, R.J. Packer, I.J. Dunkel, G. Dhall, S. Wu, A. Onar, J.M. Boyett, M. Fouladi, Phase I trial of p28 (NSC745104), a non-HDM2-mediated peptide inhibitor of p53 ubiquitination in pediatric patients with recurrent or progressive central nervous system tumors: a Pediatric Brain Tumor Consortium Study, Neuro-Oncology 18 (2016) 1319–1325, http://dx.doi.org/10.1093/neuonc/now047.

[81] M.A. Warso, J.M. Richards, D. Mehta, K. Christov, C. Schaeffer, L. Rae Bressler, T. Yamada, D. Majumdar, S.A. Kennedy, C.W. Beattie, T.K. Das Gupta, A first-in-class, first-in-human, phase I trial of p28, a non-HDM2-mediated peptide inhibitor of p53 ubiquitination in patients with advanced solid tumours, Br. J. Cancer 108 (2013) 1061–1070, http://dx.doi.org/10.1038/bjc.2013.74.

[82] N. Guex, M.C. Peitsch, Swiss-model and the Swiss-Pdb Viewer: an environment for comparative protein modeling, Electrophoresis 18 (1997) 2714–2723.